Int. J. Heat Mass Transfer. Vol. 23, pp. 1229–1241

0017-9310/80/0901-1229 $02.00/0

THE EFFECT OF TURBULENT HEAT TRANSFER ON THE PROPAGATION OF AN OPTICAL BEAM ACROSS SUPERSONIC BOUNDARY/SHEAR LAYERS*

S. E. ELGHOBASHI
University of California, Irvine, CA, U.S.A.
and
A. T. WASSEL
Thermal and Fluid Physics Division, Science Applications, Inc., El Segundo, CA, U.S.A.

(*Received* 23 *October* 1979 *and in revised form* 6 *February* 1980)

Abstract — A mathematical model is presented for predicting the turbulent and optical characteristics of supersonic boundary layers interacting with sub- and supersonic cooling wall jets. The injectant and boundary layers are of matched or unmatched pressures. In addition to the mean and fluctuating properties of the flowfield, fluctuations of the medium index of refraction and retardation of optical beams propagating through the medium are predicted. Comparisons with experimental data show good agreement.

NOMENCLATURE

C_p, specific heat at constant pressure;
c_1, c_2, c_{T_1}, c_{T_2}, c_l, c_μ, constants in the turbulence model;
H, total enthalpy;
k, kinetic energy of turbulence $= \frac{1}{2}\overline{u_i u_i}$;
l, length scale;
M, molecular weight;
n, exponent, index of refraction;
$\tilde{n}$, $1 - n$;
p, static pressure;
r, radial distance;
R, R_0, specific and universal gas constants;
t, time;
T, temperature;
u, streamwise velocity component;
v, lateral velocity component;
x, streamwise coordinate;
y, lateral distance.

Greek symbols

ε, dissipation rate of k;
μ, viscosity;
λ, wavelength;
ρ, density;
σ_H, σ_T, σ_K, σ_ε, turbulent Prandtl/Schmidt numbers;
ϕ, phase variation of optical beam;
ω, dimensionless stream function.

Subscripts

eff, effective;
j, jet;
max, maximum;
min, minimum;
s, splitter plate;
t, turbulent.

Superscripts

$\bar{}$, time-averaged value;
$'$, fluctuating component;
$+$, maximum instantaneous value;
$-$, minimum instantaneous value.

* Sponsored by Ballistic Missile Defense Advanced Technology Center under contract No. DASG60-78-C-0152.

1. INTRODUCTION

ADVANCED hypersonic flight vehicles which utilize window concepts protecting an optical or radar guidance sensor are being investigated. In order to provide cooling for optical windows, gaseous coolants are being considered where cold gas is injected through a wall slot tangentially into the vehicle boundary layer.

Sensor performance evaluation requires the understanding of the characteristics of the vehicle's hot hypersonic boundary layer over the window and its interaction with the cold wall jet. The optical designer requires detailed information on the flowfield mean and fluctuating properties and the thermodynamic state throughout the injectant, shear and boundary layers. The optical properties of the layers and, hence, the sensor's optical performance can then be evaluated.

The purpose of this paper is to present a model for predicting the flowfield characteristics over optical windows. The flow is considered turbulent, and the turbulence structure is represented by rate equations governing the kinetic energy of turbulence and its dissipation rate. The mixing streams can be subsonic or supersonic and of matched or unmatched pressures (lateral variations in the pressure distribution can exist due to imbedded shock waves). A conservation equation representing the mean square of the temperature fluctuation is included in the model, which allowed the calculation of the fluctuation of the index of refraction and refraction of optical beams. The instantaneous

temperature, index of refraction and beam phase variation were extracted from an assumed shape of the probability distribution function of the temperature fluctuation. In the present analysis the instantaneous temperature was assumed to fluctuate between a minimum and a maximum and spends no time in between.

The governing flowfield conservation equations were solved using a finite difference-marching procedure. The Semi-Implicit Method for Pressure-Linked Equations technique was utilized in the present study.

2. MATHEMATICAL ANALYSIS

The mathematical analysis presented here is based on two main elements:

(i) The solution of the transport equations of heat, mass and momentum in the turbulent compressible flow fields under consideration. These equations are listed in Section 2.1, and the solution method is described in Section 2.3.

(ii) The mathematical model which describes the interaction between the local turbulence quantities like temperature fluctuation and the refraction of an optical beam. This is discussed in Section 2.2.

2.1. *Equations of heat, mass and momentum transport*

The flows considered in the present study are steady, turbulent and two-dimensional plane or axisymmetric. The independent variables are the distances along, and perpendicular to, the predominant direction of flow. The dependent variables of the time-mean motion are the streamwise velocity, u; the lateral velocity, v; the static pressure, p; and the stagnation enthalpy, H. The conservation equations which govern the mean motion are:

$$\frac{\partial}{\partial x}(\rho u) + \frac{1}{r^n}\frac{\partial}{\partial r}(\rho v r^n) = 0. \tag{1}$$

Streamwise momentum:

$$\rho u\frac{\partial u}{\partial x} + \rho v\frac{\partial u}{\partial r} = -\frac{\partial p}{\partial x} + \frac{1}{r^n}\frac{\partial}{\partial r}\left(\mu_{\text{eff}} r^n \frac{\partial u}{\partial r}\right). \tag{2}$$

Lateral momentum (neglecting viscous terms):

$$\rho u\frac{\partial v}{\partial x} + \rho v\frac{\partial v}{\partial r} = -\frac{\partial p}{\partial r}. \tag{3}$$

Stagnation enthalpy:

$$\rho u\frac{\partial H}{\partial x} + \rho v\frac{\partial H}{\partial r} = \frac{1}{r^n}\left(\frac{\mu_{\text{eff}}}{\sigma_H} r^n \frac{\partial H}{\partial r}\right) + \frac{1}{r^n}\frac{\partial}{\partial r}\left\{r^n \mu_{\text{eff}}\left(1 - \frac{1}{\sigma_H}\right)u\frac{\partial u}{\partial r}\right\} + \frac{1}{r^n}\frac{\partial}{\partial r}\left\{r^n \mu_{\text{eff}}\left(\frac{1}{\sigma_k} - \frac{1}{\sigma_H}\right)\frac{\partial k}{\partial r}\right\}. \tag{4}$$

The temperature and density are given by the relations:

$$T = [H - \tfrac{1}{2}(u^2 + v^2) - k]/C_p \tag{5}$$

$$\rho = P/RT = RM/R_0 T \tag{6}$$

where compressibility effects are accounted for via both P and T. In the above equations, $n = 0$ for two-dimensional flow and $n = 1$ for axisymmetric flow.

The eddy viscosity μ_{eff}, which appears in the above set of equations is obtained from:

$$\mu_{\text{eff}} = \mu_t + \mu_{\text{lam}}. \tag{7}$$

The turbulent viscosity at each point in the flow is obtained from:

$$\mu_t = C_\mu \frac{\rho k^2}{\varepsilon}. \tag{8}$$

The kinetic energy of turbulent k and its dissipation rate ε are calculated from their respective conservation equations, [1]:

$$\rho u\frac{\partial k}{\partial x} + \rho v\frac{\partial k}{\partial r} = \frac{1}{r^n}\frac{\partial}{\partial r}\left(\frac{\mu_{\text{eff}}}{\sigma_k} r^n \frac{\partial k}{\partial r}\right) + \mu_t\left(\frac{\partial u}{\partial r}\right)^2 - \rho\varepsilon \tag{9}$$

$$\rho u\frac{\partial \varepsilon}{\partial x} + \rho v\frac{\partial \varepsilon}{\partial r} = \frac{1}{r^n}\frac{\partial}{\partial r}\left(\frac{\mu_{\text{eff}}}{\sigma_\varepsilon} r^n \frac{\partial \varepsilon}{\partial r}\right) + C_1\frac{\varepsilon}{k}\mu_t\left(\frac{\partial u}{\partial r}\right)^2 - C_2\frac{\rho\varepsilon^2}{k}. \tag{10}$$

The length scale of turbulence is related to k and ε by:

$$l = C_l\frac{k^{3/2}}{\varepsilon}. \tag{11}$$

The boundary conditions of the above conservation equations are discussed for each of the flows considered in Section 3.

2.2. *A mathematical model for the effect of local temperature fluctuation on the propagation of an optical beam*

An optical beam experiences a phase variation (retardation) as it propagates through a medium of nonuniform density. In a turbulent flowfield which experiences local density fluctuation (due to the local temporal fluctuation of the temperature, pressure or species concentration), the local index of refraction of the fluid consequently varies with time.

The present mathematical model predicts the fluctuation of the refractive index by relating the instantaneous value of that index to the instantaneous value of the temperature. This is accomplished as follows:

(i) The local mean square temperature fluctuation ($\overline{T'^2}$) is obtained from the solution of its conservation equation [2].

$$\rho u\frac{\partial \overline{T'^2}}{\partial x} + \rho v\frac{\partial \overline{T'^2}}{\partial y} = \frac{1}{r^n}\frac{\partial}{\partial r}\left(r^n\frac{\mu_{\text{eff}}}{\sigma_T}\frac{\partial \overline{T'^2}}{\partial r}\right)$$

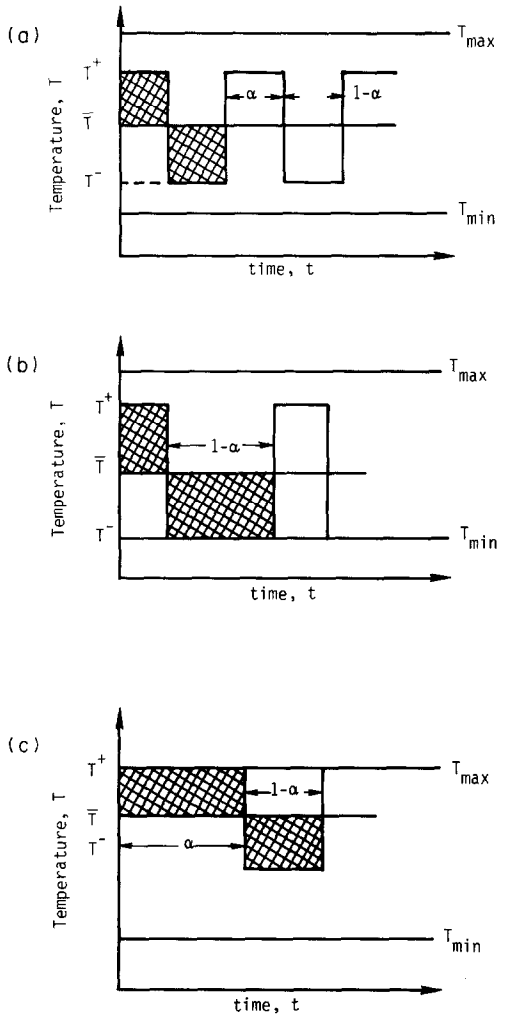

FIG. 1. Temperature–time rectangular wave.

$$+ C_{T_1}\mu_t\left(\frac{\partial T}{\partial r}\right)^2 - C_{T_2}\frac{\rho\varepsilon\overline{T'^2}}{k} \quad (12)$$

where C_{T_1} and C_{T_2} are empirical constants and σ_T is the Prandtl number of $\overline{T'^2}$.

(ii) The instantaneous temperature is assumed to follow a rectangular wave with time. This means that the probability density function of the temperature consists of only two delta functions. In general, the magnitudes of these functions are not equal. To allow for the physical realism to be incorporated in this assumption the following bounds on $T(t)$ are introduced to insure that $T(t)$ never exceeds T_{max} or drops below T_{min} (as depicted in Fig. 1).

Case A (Fig. 1a)

$$(T_{max} - \bar{T}) > \sqrt{\overline{T'^2}} \quad \text{and} \quad (\bar{T} - T_{min}) > \sqrt{\overline{T'^2}} \quad (13a)$$

$$\alpha = 0.5 \quad (13b)$$

$$T^+ = \bar{T} + \sqrt{\overline{T'^2}}, \quad T^- = \bar{T} - \sqrt{\overline{T'^2}}. \quad (13c)$$

Case B (Fig. 1b)

$$\sqrt{\overline{T'^2}} > (\bar{T} - T_{min}) \quad (14a)$$

$$T^- = T_{min} \quad (14b)$$

$$T^+ = \bar{T} + \overline{T'^2}/(\bar{T} - T^-) \quad (14c)$$

$$\alpha = (\bar{T} - T^-)/(T^+ - T^-). \quad (14d)$$

Case C Fig. 1c)

$$\sqrt{\overline{T'^2}} > (T_{max} - \bar{T}) \quad (15a)$$

$$T^+ = T_{max} \quad (15b)$$

$$T^- = \bar{T} - \frac{\overline{T'^2}}{(T^+ - \bar{T})} \quad (15c)$$

$$\alpha = 1 - \frac{(T^+ - \bar{T})}{(T^+ - T^-)}. \quad (15d)$$

The value of α at each point in the flow is determined from one of the equations (13b), (14d) and (15d) depending on the magnitude of the temperature fluctuation given by equations (13a), (14a) and (15a).

In all these three cases the time mean density $\bar{\rho}$ is calculated from:

$$\bar{\rho} = \alpha\rho^+ + (1-\alpha)\bar{\rho} = \frac{pM}{R_0}\left[\frac{\alpha}{T^+} + \frac{(1-\alpha)}{T^-}\right], \quad (16a)$$

and the mean-square of the density fluctuation is given by

$$\overline{\rho'^2} = (\rho^+ - \bar{\rho})(\bar{\rho} - \rho^-). \quad (16b)$$

More realistic probability density functions can be readily incorporated into the above model when detailed experimental data for the temperature fluctuation in turbulent shear flows become available.

(iii) The instantaneous values of the refractive index, n, is calculated from the empirical relation [3]:

$$n(t) = 1 + \frac{77.6\,p}{T(t)}\left[1 + \frac{0.00753}{\lambda^2}\right] \times 10^{-6} \quad (17)$$

where p is the pressure in mb, λ is the wavelength in μm and T is the instantaneous temperature in K. Equation (17) shows that n is inversely proportional to T. It then follows that the maximum value of n, n^+, will correspond to the minimum value of T, T^-, and vice versa. The quantity $\bar{n}$ is obtained from $\bar{n} = \alpha n^+ + (1-\alpha)n^-$.

A quantity of practical interest is the phase variation of an optical beam which propagates through a gaseous medium of variable (in space and time) index of refraction n. The instantaneous phase variation $\phi(t)[2\pi/\lambda]$ can be calculated from the optical path length $\phi(t)$ as follows [4]:

$$\phi(t) = \int [n(t) - 1]\,ds, \quad (18)$$

where s is the optical path and $(2\pi/\lambda)$ is the wavenumber in vacuum.

According to equation (18), the maximum instantaneous value ϕ^+ is proportional to n^+, and the minimum value ϕ^- is proportional to n^-. The time-mean value of the phase variation $\bar{\phi}$ is obtained from:

$$\bar{\phi} = \bar{\phi}(\bar{n}) \tag{19}$$

The root-mean-square value of ϕ is given by

$$\sqrt{\overline{\phi'^2}} = \sqrt{[(\phi^+ - \bar{\phi})(\bar{\phi} - \phi^-)]}. \tag{20}$$

2.3. *The solution procedure*

A finite difference procedure of the marching (from upstream to downstream) integration type is used to solve the set of conservation equations (1)–(4), (9), (10) and (12). This procedure is described in detail in [5] and will be only briefly outlined in this section. The governing set of differential equations is first transformed into a stream function plane (x, ω) using a Von Mieses type transformation. The finite difference grid adopted is similar to that of [5].

The SIMPLE (Semi-Implicit Method for Pressure-Linked Equations) algorithm [5] is used to link the streamwise and lateral momentum equations with the continuity equation so as to obtain a pressure field. This linkage is necessary in supersonic or transonic flows where the assumption of uniform pressure in the lateral direction is invalid.

3. RESULTS AND DISCUSSION

This section presents the predicted results and compares them, whenever possible, with existing experimental data or results of other numerical procedures. Four flows are considered here. These are:

(i) An axisymmetric underexpanded jet issuing in a confined supersonic flow;
(ii) Unmatched-pressure supersonic injection from a 2-D wall-slot into a supersonic free stream;
(iii) Matched-pressure supersonic injection from a 2-D wall-slot into a supersonic free stream;
(iv) Matched-pressure subsonic injection from a 2-D wall-slot into a supersonic free stream.

The third and fourth flows provide the only available experimental data to validate the predictions of the phase variation of an optical beam. Testing was performed at AF-FDL Mach-3 wind tunnel [6], where both optical (holographic interferometry) and probe (hot wire anemometry and Pitot and static pressure probes) measurements were obtained.

3.1. *Computational details*

The conservation equations contain empirical constants to which values must be assigned. The values of these constants were inferred by comparisons with experimental data of simple flow configurations [7]. Presented in Table 1 are the values of these constants used in the computations. The finite-difference grid employed in the present computation consists of 50 cells in the y-direction at any given streamwise station.

Table 1. Values of empirical constants

Dependent variable	Constant	Value
H	σ_H	0.9
k	σ_k	1.0
ε	σ_ε	1.09
	C_1	1.43
	C_2	1.92
$\overline{T'^2}$	σ_T	0.7
	C_{T_1}	2.8
	C_{T_2}	1.4
μ_t	C_μ	0.09
l	C_l	0.164

The optimum size of the forward step is determined by the solution procedure at each new step to eliminate any numerical instability and to ensure economy. The computations were performed on a CDC-7600. The core storage required during execution is 103 K (octal) and the CPU time for one step is 0.006 s.

3.2. *Axisymmetric jet issuing in a confined supersonic flow*

3.2.1. *Flow description.* The flow configuration is shown in Fig. 2, and the conditions at the exit plane are summarized in Table 2.

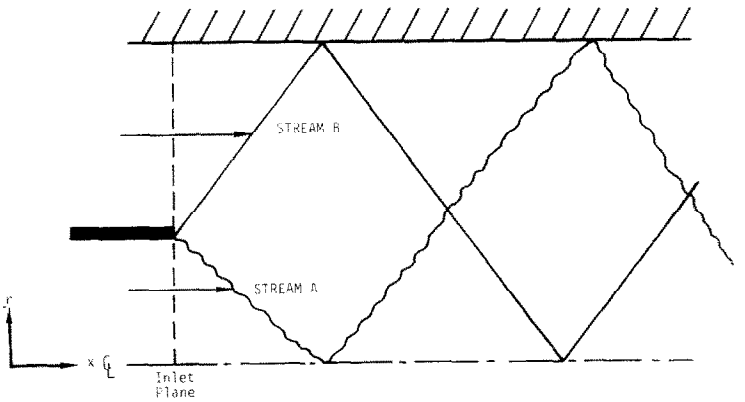

FIG. 2. Configuration of the two coaxial supersonic jets.

Table 2. Flow conditions at the exit plane of confined axisymmetric jet and 2-D wall jet

	Axisymmetric confined jet		2-D wall jet	
	Stream A	Stream B	Stream A	Stream B
Fluid	Air	Air	Air	Air
u ($m\,s^{-1}$)	1330.0	2625.0	490.7	691.0
v ($m\,s^{-1}$)	0.0	0.0	0.0	0.0
M	2.0	3.38	1.98	4.19
p ($10^5\,N\,m^{-2}$)	1.0	0.5	2.5	1.0
r, y (m)	0.001	0.00376	0.0135	0.01986
T(K)	1100.0	1500.0	180.6	79.96

This flow was predicted by Kurkov [8], using a finite difference procedure. He treated the flow as inviscid and the stream B fluid was hydrogen. In this case the fluid is air and the flow is treated as laminar; otherwise, the inlet conditions are identical to that of Kurkov.

3.2.2. *Boundary conditions.* The present marching-integration procedure requires the specification of the boundary conditions along the axis and the confining wall. The gradients in the r-direction of all the dependent variables vanish at the axis. At the wall, the no-slip condition is enforced.

3.2.3. *Results.* Figure 3 shows the predicted pressure distribution along the axis of symmetry, together with that calculated by Kurkov [8]. The main features are well predicted: the locations of the expansion wave (at $x/r_j \simeq 3$) and the reflection of the shock (at $x/r_j \simeq 18$). The predicted value of the maximum pressures are in very good agreement. The value of the minimum pressure at $x/r_j = 3$ is overpredicted by approximately 67%. The grid used here includes 50 cells in the radial direction. A finer grid would probably improve the predictions at the pressure dip. In addition, plug profiles were assumed for both streams at the inlet plane.

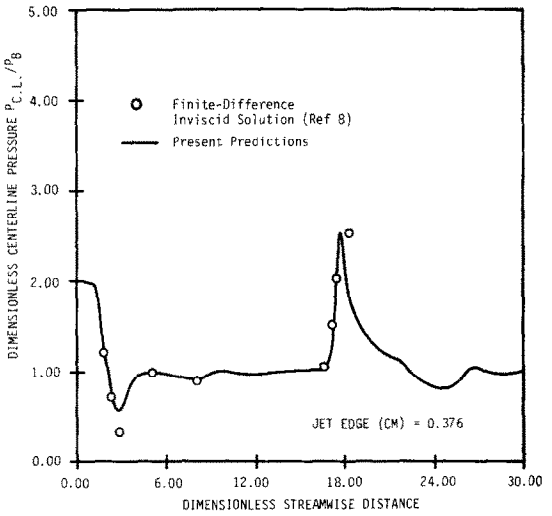

FIG. 3. Pressure distribution along the centerline of the coaxial jets.

3.3. *Unmatched-pressure, turbulent, supersonic injection from a 2-D wall-slot into a supersonic free stream*

3.3.1. *Flow description.* Figure 4 shows a schematic of the flow considered, and Table 2 summarizes the conditions at the exit plane of the slot. A supersonic wall jet issues into a lower pressure, faster moving stream. The conditions of this flow are those of the experiment of Schetz *et al.* [9].

3.3.2. *Boundary conditions.* Near the wall, turbulent wall functions [10] are used to calculate the shear stress, the kinetic energy of turbulence and its dissipation rate. At the edge of the supersonic free stream (i.e. at the last finite-difference cell in the free stream) the assumption of the simple wave is employed [5] to calculate u, v, p there.

3.3.3. *Results.* Figure 5 displays a comparison between the predicted and measured [9] pressure distribution along the wall. The agreement is good except that the trough of the pressure is about 20% higher than the measured one. This is the location of the interaction of the expansion wave with the wall.

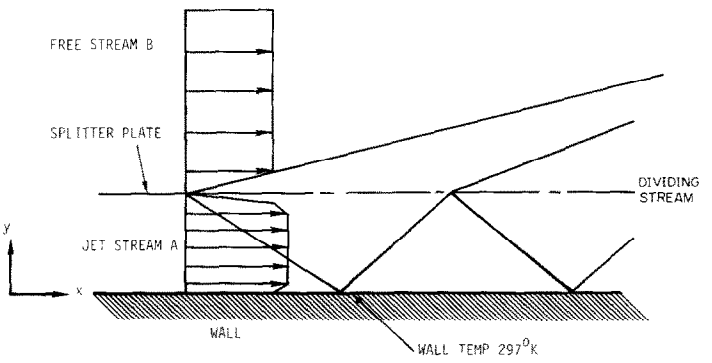

FIG. 4. Wall-slot jet injected into free stream.

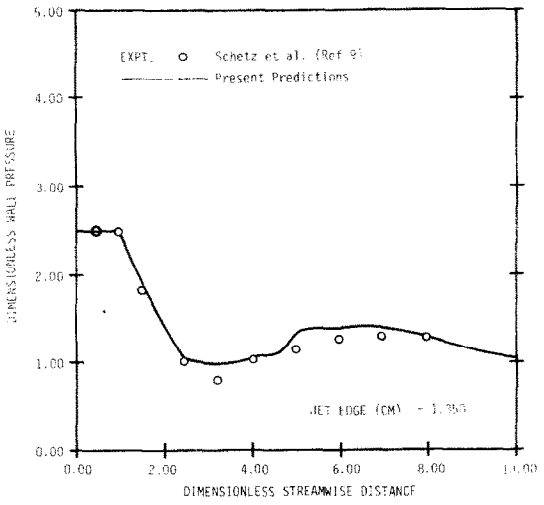

FIG. 5. Pressure distribution along the wall.

It should be noted that the present predicted pressure distribution is in better agreement with the data than those of [11]. This is due to the prescribed profiles used here of u, p, T, ρ at the exit of the slot which take an account of the boundary layers on both the slot walls and the splitter plate. Reference [11] assumed plug profiles. In the present study 1/7th power law profiles were used.

3.4. *Matched-pressure supersonic injection from a 2-D wall-slot into a supersonic free stream*

3.4.1. *Flow description.* The flow configuration of this case is identical to that of the unmatched-pressure case (Fig. 4). The conditions at the exit plane of the slot are given in Table 3. The blowing rate is about $0.775\,\mathrm{kg\,m^{-1}\,s^{-1}}$. The slot height y_s is 0.0064 m. The wall temperature is 274 K.

3.4.2. *Boundary conditions.* The boundary conditions here are the same as in the unmatched pressure case (Section 3.3).

3.4.3. *Results.* Figures 6 to 11 show a comparison between the predicted and measured flow properties at the streamwise stations of $x/y_s = 4.33, 8.03$ which will be referred to hereafter as Stations I and II, respectively.

3.4.4. *Time-mean velocity.* The profiles of the time-mean velocity are displayed in Fig. 6. The predictions and measurements are in good agreement at the two stations. The growth of the shear layer, indicated by the vanishing of the dip in the velocity profile at $y/y_s \approx 1.1$, is well predicted. The velocity in the inner region ($y/y_s < 0.9$) is overpredicted by about 6%; this discrepancy is within the limits of the experimental accuracy.

3.4.5. *Mach number.* Figure 7 shows the distributions

Table 3. Conditions at the exit plane of the slot for the supersonic and subsonic injection cases

	Supersonic injection		Subsonic injection	
	Stream A	Stream B	Stream A	Stream B
Fluid	Air	Air	Air	Air
$u\ (\mathrm{m\,s^{-1}})$	455.0	570.0	202.0	470.0
$v\ (\mathrm{m\,s^{-1}})$	0.0	0.0	0.0	0.0
M	1.66	2.79	0.622	2.79
$p\ (10^5\,\mathrm{N\,m^{-2}})$	0.145	0.145	0.145	0.145
T (K)	180.0	100.0	253.0	100.0

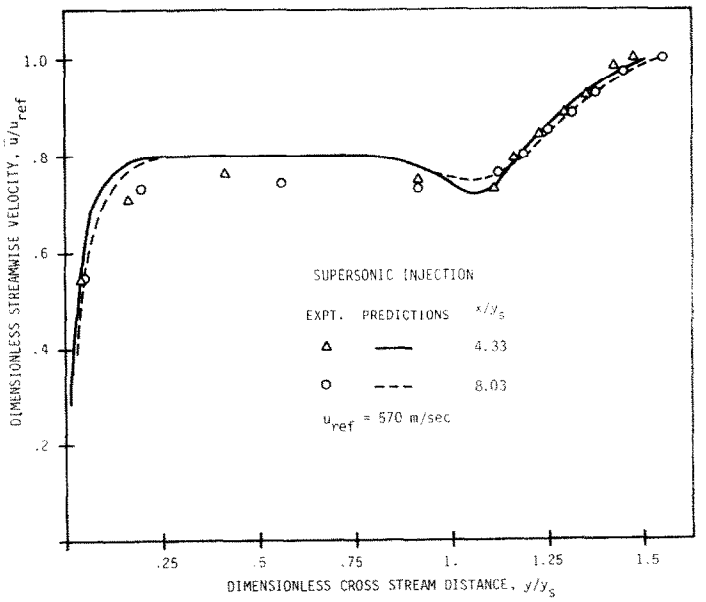

FIG. 6. Lateral distribution of streamwise time-mean velocity.

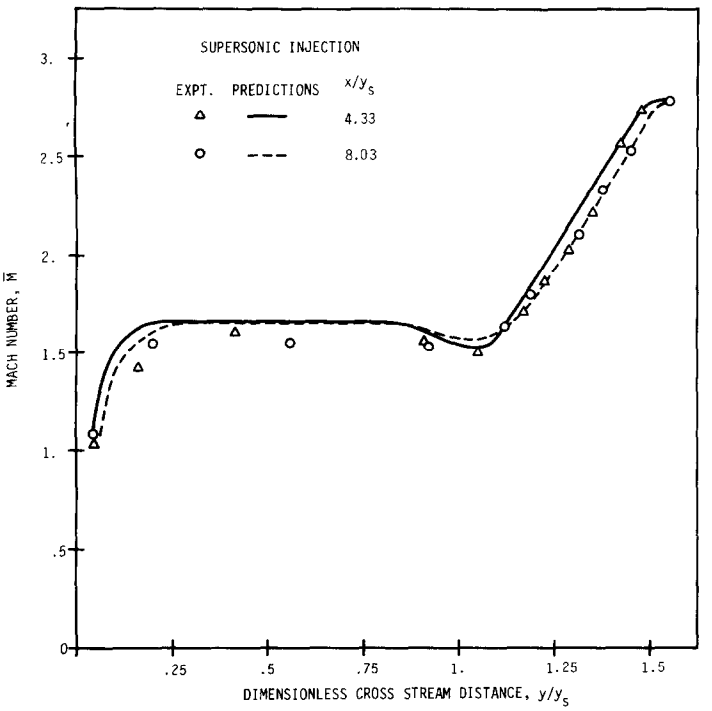

FIG. 7. Lateral distribution of streamwise time-mean Mach number.

of the Mach number in the radial direction at the two stations. The agreement is good between the predictions and experiment in the shear layer and in the outer flow. Again, the Mach number is overpredicted by about 6% in the inner region.

3.4.6. *Time-mean temperature.* Figure 8 depicts the two profiles of the time-mean temperature. In contrast with the velocity profiles, the temperature profiles are well-predicted in the inner region (up to $y/y_s = 0.9$). In the outer region, a discrepancy of about 10% exists between the measurements and the predictions. This underprediction of the temperature may be caused by the high value of the constant turbulent Prandtl number used ($\sigma_H = 0.9$) in the solution procedure. Both the predictions and experiment show a slight increase in temperature with downstream distance for $y/y_s > 1.25$.

3.4.7. *Time-mean density.* Figure 9 shows the profiles of the time-mean density. The agreement between the predictions and measurement at the station of $x/y_s = 8.02$ is good and is fair for Station I. The underpredicted density at that station in the outer region

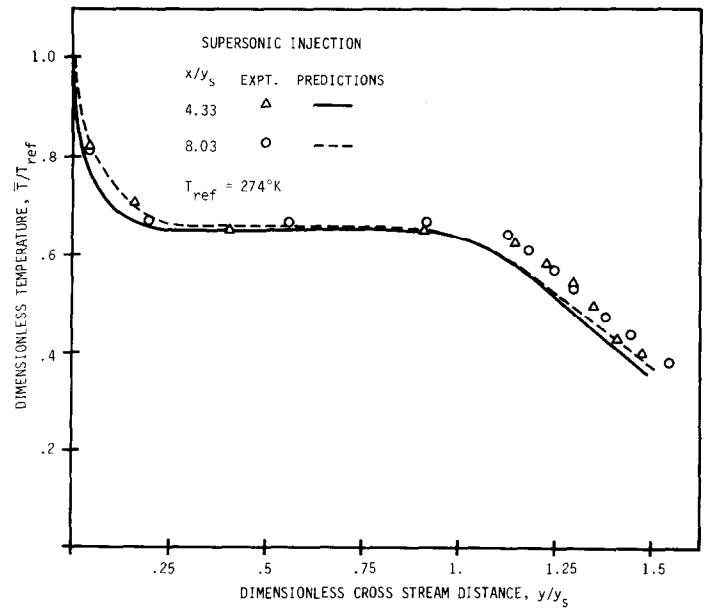

FIG. 8. Lateral distribution of time-mean temperature.

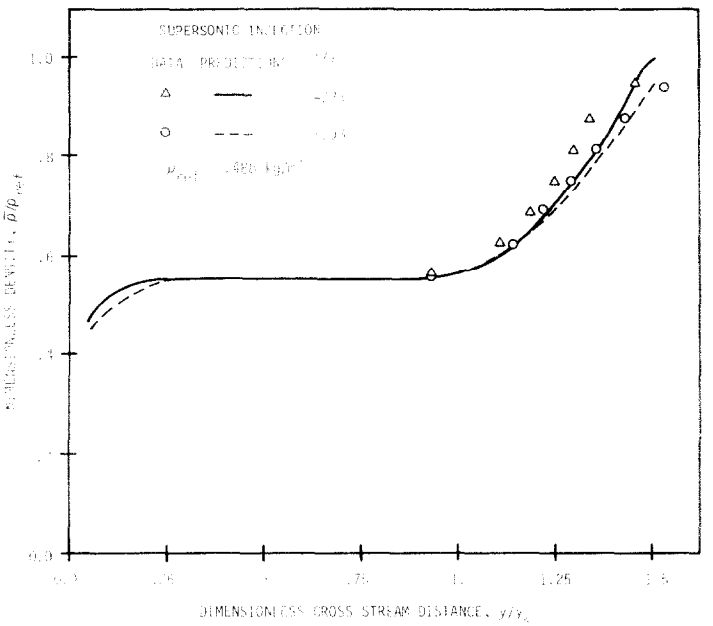

FIG. 9. Lateral distribution of mean density.

($y/y_s > 1$) suggests inaccuracies in the experimental measurements. This is because the temperature was underpredicted in that region (Fig. 8) and, consequently, the equation of state for a constant pressure should overestimate the predicted density. (In other words, we cannot underpredict both T and ρ.) No measurements of the density are available for the inner region. Both the predictions and experiment show a slight drop in density with downstream distance for $y/y_s > 1.25$.

3.4.8. *The density fluctuation.* The profiles of the density fluctuation are plotted in Fig. 10. Qualitatively, the predictions and the measurements exhibit, as expected, a peak in density fluctuations at the location ($y/y_s \approx 1.25$) of maximum density gradient (Fig. 9). The predictions are in better agreement with the hot-wire measurements at Station II than at Station I. However, the data obtained from the optical measurements agree better with the predictions.

3.4.9. *Time-mean index of refraction* ($\bar{n}$). Figure 11 shows a comparison between the optically measured and predicted profiles of the index of refraction $\bar{n}$ where, $\bar{n} = n - 1$. As indicated by equation (17), $n(t)$ is inversely proportional to $T(t)$ and, consequently, the accuracy of the prediction of $\bar{n}$ depends on how well $\bar{T}$ and $\overline{T'^2}$ are predicted. As indicated in Fig. 11 the agreement between the prediction and experiment is good.

3.4.10. *The optical beam phase variation* (ϕ). Equations (18) and (19) were used to predict ϕ^+, ϕ^- and $\bar{\phi}$. Table 4 contains the predicted values at the two Stations I and II, together with the experimental values of $\sqrt{\overline{\rho'^2}}/\lambda$ where λ is the wavelength ($\lambda = 0.69\ \mu$m). It is seen that the time-mean value and the fluctuation of the phase retardation increase with distance from the slot exit. This is mainly due to the higher density (or temperature) fluctuations at the downstream station. Also, the predictions and experiment are in good

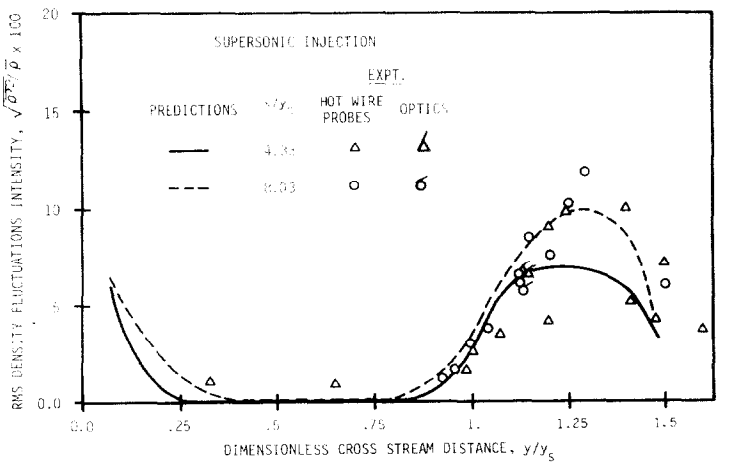

FIG. 10. Lateral distribution of density fluctuation.

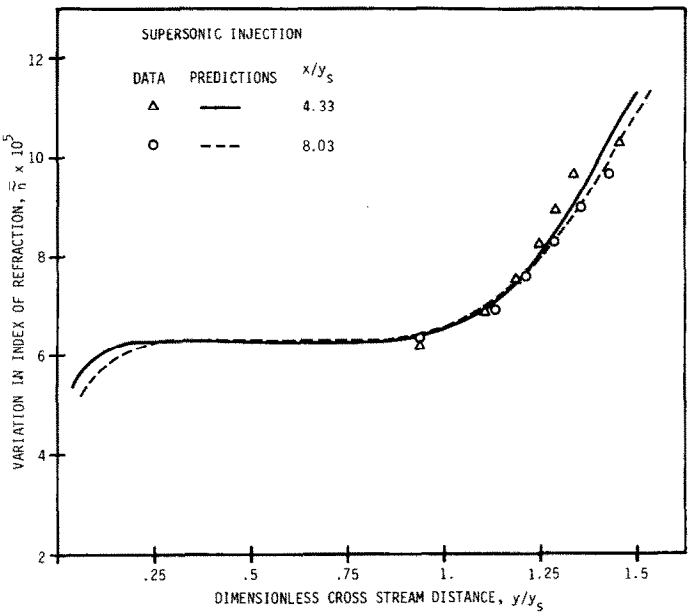

FIG. 11. Lateral distribution of mean index of refraction (optical data).

Table 4. Comparison between predictions and data of beam phase variation for supersonic and subsonic injection cases

Case	Station	x/y_s	$10^7 \times \phi^+$	$10^7 \times \phi^-$	$10^7 \times \bar{\phi}$	$\sqrt{\sigma'^2}/\lambda$ Exp.	$\sqrt{\sigma'^2}/\lambda$ Pred. (equation 17)
Supersonic	I	4.33	6.67	6.26	6.46	0.02	0.03
Supersonic	II	8.03	6.79	6.22	6.51	0.043	0.041
Subsonic	I	4.33	5.05	4.56	4.81	0.094	0.053
Subsonic	II	8.03	5.17	4.35	4.76	0.039	0.059

agreement, especially at Station II, which is due to better agreement between predictions and measurements for the quantities $\bar{\tilde{n}}$ and $\sqrt{\rho'^2}$.

3.5. Matched pressure subsonic injection from a 2-D wall slot into a supersonic stream

3.5.1. *Flow description.* The flow configuration is identical to that of the supersonic injection case (Fig. 4). The conditions at the exit plane of the slot are given in Table 3. The blowing rate for this case is $0.247\,\mathrm{kg\,m^{-1}\,s^{-1}}$.

3.5.2. *Boundary conditions.* The boundary conditions for this case are the same as in the unmatched pressure case (Section 3.3).

3.5.3. *Results.* The predicted results at the two streamwise stations ($x/y_s = 4.33, 8.03$) are presented in Figs. 12 to 16. The experimental data are plotted in Figs. 14–16. Because of the unavailability of hot wire and pressure probes experimental data, the predictions will be only qualitatively discussed, except for the density and the refractive index which were obtained from optical measurements.

3.5.4. *Time–mean velocity.* Figure 12 shows the profiles of the time–mean velocity at the two stations. The growth of the shear layer is indicated by the decreasing velocity gradient. It is seen that the width of the shear layer at $x/y_s = 8.03$ is almost three times the width of the shear layer in the supersonic injection case (Fig. 6).

3.5.5. *The time–mean temperature.* Figure 13 displays the predicted profiles of the time–mean temperature at the two stations. It is interesting to compare the rate of temperature change with streamwise distance in the shear layer in the *supersonic* and *subsonic* injection cases. Figures 8 and 13 show that in the former case the temperature almost remains constant between the two stations, whereas in the latter case a drop of about 7% is observed for $0.6 < y/y_s < 1.25$. This is attributed to the faster rate of growth of the shear layer in the subsonic case (Fig. 12), which is caused by the turbulent mixing. A larger rate of turbulent mixing would increase the rate of entrainment of the free stream fluid into the shear layer and, thereby, enhances the rate of temperature drop in that region and hence a rise in density.

In the wall region, however, the supersonic injection produces larger temperature and velocity gradients than in the subsonic injection case. Consequently, the turbulent boundary layer grows faster in the former than in the latter case. Hence, the temperature rise in

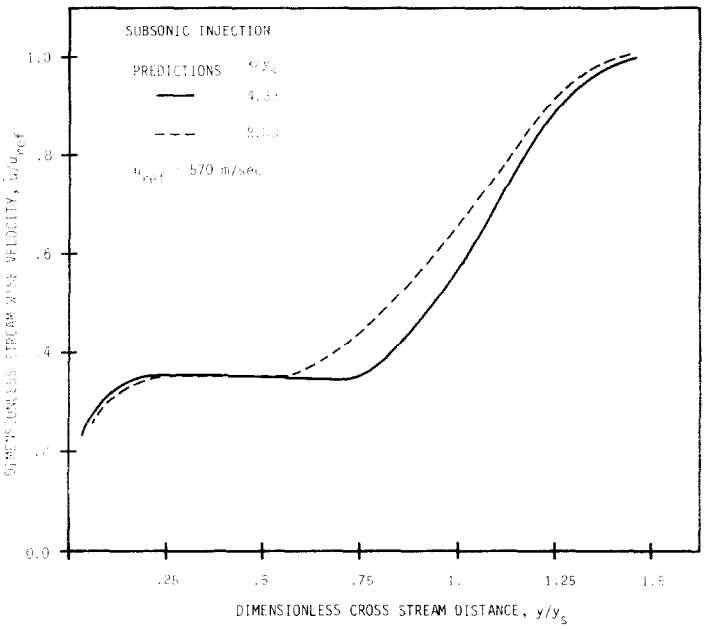

FIG. 12. Lateral distribution of streamwise mean velocity.

the wall region (between the two stations) is more in the supersonic case than in the subsonic case.

3.5.6. *The time–mean density and density fluctuation.* Figures 14 and 15 show the profiles of the density and its fluctuation intensity. The predicted density behavior is consistent with the predicted temperature (Fig. 13); a drop of the temperature with downstream distance in a uniform pressure field causes a density rise particularly away from the wall. The experimental data, however, shows a drop in density (i.e. a rise in temperature) with streamwise distance for $y/y_s > 1.0$. This trend contradicts the predictions. This may be due to the large value of σ_H (0.9) used in the computation.

Figure 15 shows a significant increase in the predicted density fluctuations with streamwise distance. This is due to an order of magnitude increase in the effective viscosity in the shear layer. Although there is a fair agreement between predictions and experiment at Station I, there are insufficient experimental data points to justify a meaningful comparison. The experimental data, however, exhibits a decrease in density and a decay of its fluctuation intensity with distance. A plausible cause of this discrepancy is that the prescribed profiles of the flow properties at the exit plane of the slot are not consistent with the actual flow conditions. To resolve this issue, more detailed experimental data are required.

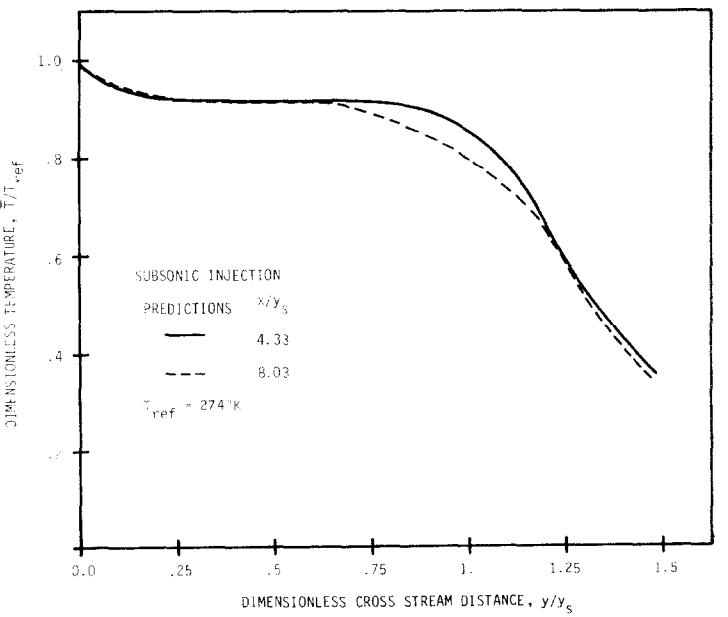

FIG. 13. Lateral distribution of mean temperature.

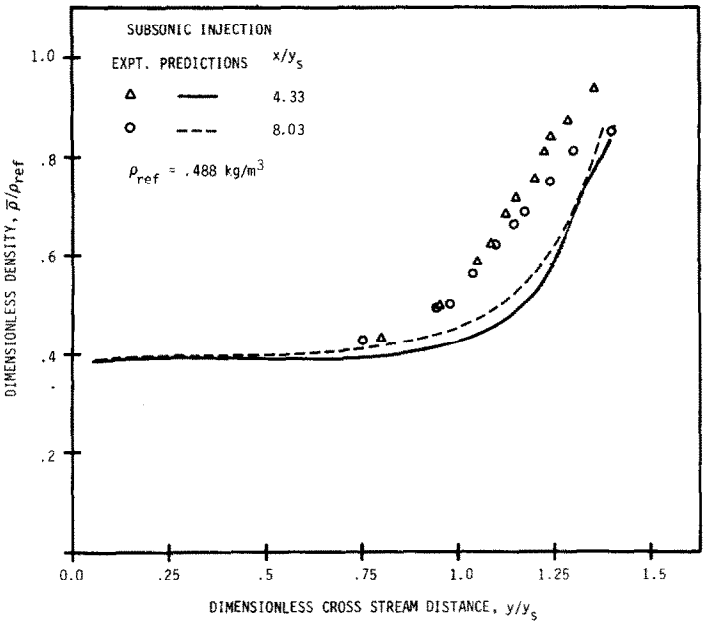

FIG. 14. Lateral distribution of mean density (optical data).

3.5.7. *The time–mean index of refraction.* Figure 16 displays the profiles of the time–mean index of refraction at the two stations. Since the index of refraction is a function of the local density, the discrepancy (explained earlier) between the measured and predicted density is reflected here again in the disagreement between the measured and predicted index of refraction.

3.5.8. *The fluctuation in the phase variation.* Table 4 contains the predicted and measured values of $\sqrt{\overline{\phi'^2}}/\lambda$ and of the predicted ϕ^+, ϕ^-, and $\bar{\phi}$ ($\lambda = 0.69\,\mu$m). Since the phase variation ϕ is a function of n, the discrepancy discussed earlier appears here also: the data indicate a drop in the value $\sqrt{\overline{\phi'^2}}$, and the predictions show an increase.

4. SUMMARY AND CONCLUSIONS

1. This manuscript has described a numerical method for predicting two-dimensional viscous compressible turbulent flows with values of Mach numbers ranging from 0.62 to 4.19.

2. A mathematical model is provided for calculating the influence of the turbulent heat transfer in boundary or shear layers on the propagation of optical beams across these layers.

3. Good agreement is achieved between the predictions and the available experimental data except for the subsonic injection case where the agreement is fair.

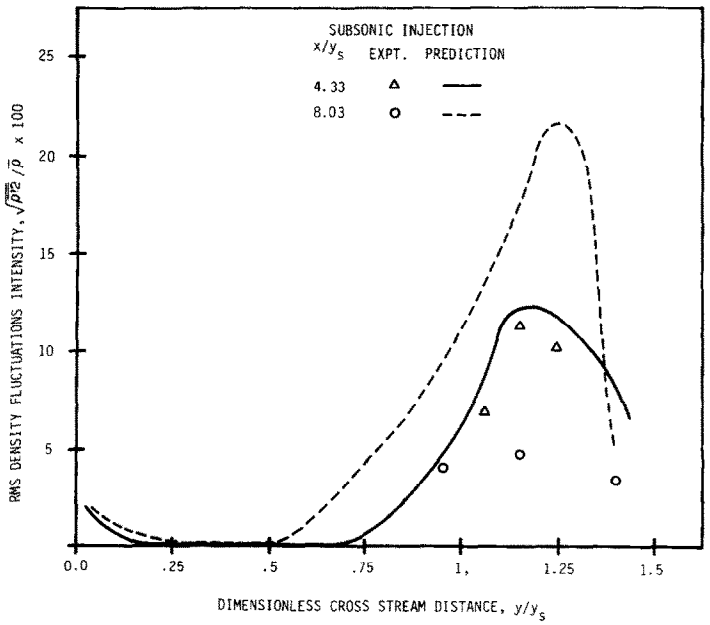

FIG. 15. Lateral distribution of density fluctuation (optical data).

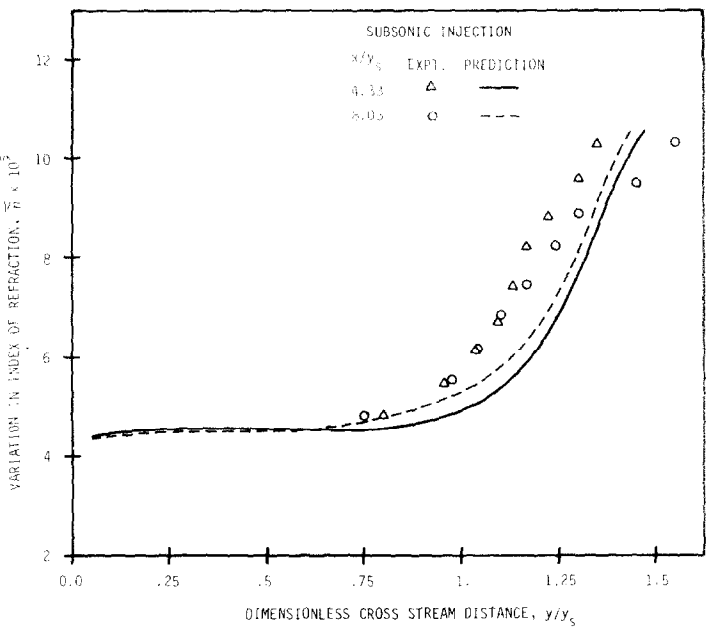

FIG. 16. Lateral distribution of index of refraction (optical data).

4. Detailed experimental data at various flow conditions are needed (different pressure ratios) to extend the validity of the procedure.

Acknowledgement — This work was performed for BMDATC under contract DASG60-78-C-0152. The BMD project monitor was Mr J. G. Papadopoulos. The SAI program manager was Dr W. C. L. Shih. Thanks are due to Drs W. C. L. Shih and J. Craig and Mr W. McKenly for supplying the AFFDL test data, and to Mr J. Farr for performing the computer calculations.

REFERENCES

1. W. P. Jones and B. E. Launder, The predictions of laminarization with a two-equation model of turbulence, *Int. J. Heat Mass Transfer* **15**, 301–317 (1972).
2. D. B. Spalding, Concentration fluctuations in a round turbulent free jet, *Chem. Engng Sci.* **26**, 95–107 (1971).
3. H. Gamo and A. K. Majumdar, Atmospheric turbulence chamber for optical transmission experiment: Characterization by thermal method, *Appl. Optics* **17**, 3755–3762 (1978).
4. J. D. Trolinger, Laser instrumentation for flow field diagnostics, AGARDograph No. 185, 1974.
5. S. E. Elghobashi and D. B. Spalding, Equilibrium chemical reaction of supersonic hydrogen-airjets, NASA CR-2725 (1977).
6. W. C. L. Shih, *et al.*, Turbulent analysis of a cooled boundary layer: Pretest report and test plan, SAI-063-80R-024-LA, May (1979).
7. B. E. Launder and D. B. Spalding, *Mathematical Models of Turbulence*, Academic Press, New York (1972).
8. A. P. Kurkov, Mixing of supersonic jets including the effects of transverse pressure gradients using different methods, NASA TN-6592, Lewis Research Center, Cleveland, Ohio (1971).
9. J. A. Schetz, *et al.*, Research on slot injection into a supersonic air stream, Rep. Aero-68-1, Maryland University (1968).
10. D. B. Spalding, GENMIX: A general computer program for two-dimensional parabolic phenomena, Imperial College of Science and Technology, HTS/77/9 (1977).
11. R. I. Issa and F. C. Lockwood, A hybrid marching integration procedure for the prediction of two-dimensional supersonic boundary layers, *J. Fluid Engng* **99**, 205–212 (1977).

LES EFFETS DU TRANSFERT THERMIQUE TURBULENT SUR LA PROPAGATION D'UN RAYON OPTIQUE A TRAVERS DES COUCHES LIMITES SUPERSONIQUES

Résumé— Un modèle mathématique est présenté pour prédire les caractéristiques turbulentes et optiques des couches limites supersoniques en intéraction avec des jets sub-ou-supersoniques refroidissant une paroi. En plus des propriétés moyennes et fluctuantes de l'écoulement, des fluctuations de l'indice de réfraction du milieu et du retard optique de la propagation de la lumière sont prédits. Des comparaisons avec des données expérimentales montrent un bon accord.

DER EINFLUSS TURBULENTER WÄRMEÜBERTRAGUNG AUF DIE FORTPFLANZUNG EINES OPTISCHEN STRAHLS IN ÜBERSCHALLREIBUNGSGRENZSCHICHTEN

Zusammenfassung—Es wird ein mathematisches Modell zur Bestimmung der strömungstechnischen und optischen Eigenschaften von Überschallgrenzschichten beschrieben, die mit kühlenden Unter- und Überschallwandstrahlen zusammenwirken. Das eingespritzte Medium und die Grenzschichten haben gleichen bzw. verschiedenen Druck. Außer den Mittelwerten und den Änderungen der Eigenschaften des Strömungsfeldes werden auch die Änderungen des mittleren Brechungsindex und der Nacheilung der optischen Wellen, die sich durch das Medium fortpflanzen, vorausberechnet. Vergleiche mit experimentell ermittelten Werten zeigen eine gute Übereinstimmung.

ВЛИЯНИЕ ТУРБУЛЕНТНОГО ПЕРЕНОСА ТЕПЛА НА ПРОХОЖДЕНИЕ СВЕТОВОГО ПУЧКА ЧЕРЕЗ СВЕРХЗВУКОВЫЕ ПОГРАНИЧНЫЕ СДВИГОВЫЕ СЛОИ

Аннотация — Представлена математическая модель для расчета турбулентных и оптических характеристик сверхзвуковых пограничных слоев, взаимодействующих с до- и сверхзвуковыми пристенными струями охлаждающей жидкости. Инжектируемая жидкость и пограничные слои находятся или при одинаковом, или разном давлении. Кроме средних и пульсационных свойств поля течения рассчитаны флуктуации показателя преломления среды и изменение оптических характеристик пучков, проходящих через среду. Получено хорошее совпадение с экспериментальными данными.